Nanoscale Advances

ROYAL SOCIETY OF CHEMISTRY

PAPER

View Article Online
View Journal | View Issue

Cite this: *Nanoscale Adv.*, 2025, **7**, 6640

Synergistic selenium vacancies and bismuth metal centers on Bi_2Se_3 for enhanced photocatalytic CO_2 reduction

Yanjun Zhu, [ab] Qiutong Han [*c] and Yong Zhou [*abd]

Received 29th May 2025
Accepted 17th August 2025

DOI: 10.1039/d5na00526d

rsc.li/nanoscale-advances

Ultrathin inorganic nanosheets possess a novel electronic structure that enables exceptional performance in the catalytic reduction of carbon dioxide (CO_2), representing a promising strategy to mitigate global warming. Bismuth selenide (Bi_2Se_3) nanosheets are important topological insulators exhibiting high electrical conductivity. Through a solvothermal method followed by hydrogen annealing, selenium-vacancy-rich Bi_2Se_3 nanosheets with *in situ* formed bismuth metal clusters are prepared. In this system, surface Se vacancies function as active centers for electron trapping and CO_2 adsorption, while Bi metal clusters serve as reactive sites to facilitate charge transfer and catalytic reactions. This dual-functional design establishes a unidirectional electron transfer pathway from selenium vacancies to Bi metal through the topological conductive surface, thereby concentrating electrons at the Bi interface and providing abundant reducing equivalents to enhance CO yield.

1 Introduction

The excessive consumption of fossil fuels has led to an energy crisis and climate change, posing a severe challenge to the sustainable development of humanity.[1–3] Although photocatalytic CO_2 reduction technology is regarded as a solution, the current systems still face key scientific issues such as low solar energy utilization efficiency, high reaction energy barriers, and slow kinetic processes, resulting in a relatively low conversion efficiency of CO_2. Ultrathin inorganic nanosheets have the same structure as graphene and possess a novel electronic structure, thus exhibiting excellent physical and chemical properties.[4,5] With abundant surface atoms exposed, they are prone to forming a lot of defects/vacancies.[6] Even at extremely low defect concentrations, the electronic structure changes significantly. Recent studies have shown that the type and concentration of defects/vacancies greatly affect the catalytic performance of two-dimensional nanomaterials. For example, when there are S vacancies on the surface of $AgInP_2S_6$ ultrathin nanosheets, the main product of the catalytic reaction changes from carbon monoxide to ethylene.[7] This means that sulfur vacancy engineering on this atomic layer can significantly change the CO_2 photocatalytic reduction reaction pathway. Meanwhile, defects/vacancies can provide more active sites and enhance catalytic activity. For instance, rose-shaped BiOCl with bismuth vacancy assemblies provides a lot of adsorption and catalytic sites, enhancing its ability to capture and reduce CO_2.[8] However, the identification and quantification of vacancies in topological insulators are still poorly understood at present, which limits the rational design of defect-engineered catalysts.

Bismuth selenide (Bi_2Se_3), as a typical topological insulator, provides a good platform for solving the above problems.[9] Bismuth-based materials have long been employed in catalytic applications,[10,11] with bismuth selenide (Bi_2Se_3) demonstrating particularly unique properties. Specifically, its electronic band gap is closely related to the thickness and can be tuned between the insulating and conducting states. Moreover, even in the presence of defects, due to topological protection, Bi_2Se_3 still exhibits strong surface conductivity under environmental conditions. The surface defects of Bi_2Se_3 produce topological dangling bonds, providing a lot of sites for atom or molecule adsorption and endowing it with high chemical activity.[12] However, research on the identification and quantification of defects in topological insulators is relatively scarce. Therefore, tuning the thickness of Bi_2Se_3 and constructing Se vacancies as electron capture centers is expected to improve the kinetic process of the photocatalytic CO_2 reduction reaction.[13,14]

In addition, in photocatalytic CO_2 reduction, metals can significantly enhance catalytic performance by providing active sites, promoting charge separation, and regulating reaction pathways. For example, Cu/TiO_2 enhances CO_2 activation by enriching electrons,[15] Au/ZnO suppresses carrier recombination

[a]*National Laboratory of Solid State Microstructures, Collaborative Innovation Center of Advanced Microstructures, School of Physics, Nanjing University, Nanjing 210093, P. R. China. E-mail: zhouyong1999@nju.edu.cn*

[b]*Eco-Materials and Renewable Energy Research Center (ERERC), Jiangsu Key Laboratory for Nano Technology, Nanjing University, Nanjing, 210093, P. R. China*

[c]*State Key Laboratory of Materials-Oriented Chemical Engineering, School of Physical and Mathematical Sciences, Nanjing Tech University, Nanjing, Jiangsu, 211816, P. R. China. E-mail: hanqt@njtech.edu.cn*

[d]*School of Science and Engineering, The Chinese University of Hongkong (Shenzhen), Shenzhen 518172, P. R. China*

through heterojunctions,[16] and Ag/g-C_3N_4 improves product selectivity by optimizing intermediate adsorption.[17] Compared with precious metals, single-atom Bi has the advantages of low cost, low toxicity, and high stability. Taking metallic bismuth (or bismuth clusters) as an efficient active center, the material is endowed with broad-spectrum visible light responsiveness by its inherent narrow band gap (~2.3 eV).[18] Meanwhile, the strong electron coupling interaction formed with the carrier (such as Bi_2Se_3) can directionally guide the migration of photogenerated electrons. Specifically, Se vacancies act as electron capture centers[19–21] and metal Bi acts as an electron sink and catalytic hotspot, synergistically suppressing charge recombination.[22,23] Indeed, incorporating recent advances in defect engineering and bimetallic catalysts can synergistically enhance the efficiency of photocatalytic CO_2 reactions.[24–26] This bifunctional configuration establishes a unidirectional electron transfer pathway from selenium vacancies to Bi metal through the topological conductive surface-thereby concentrating electrons at the Bi interface and providing abundant reducing electrons for photocatalytic CO_2 reduction.[27]

In this paper, flake-structured Bi_2Se_3 materials were synthesized by the solvothermal method. After hydrogen annealing treatment, a lot of Se vacancies were generated in the materials, and some of the Bi elements were reduced to Bi monomers, forming Bi metal clusters. Photogenerated electrons were captured by Se defects and transported to Bi monomers through the excellent conductivity of the Bi_2Se_3 surface. This tandem mechanism effectively realizes the separation of electrons and holes. Meanwhile, metal Bi and selenium defects synergistically enhance the chemical adsorption and activation of CO_2, reduce the reaction energy barrier,[28,29] and increase the CO yield by nearly 27.36 times compared with the original Bi_2Se_3. This work provides a new idea for constructing an efficient and sustainable photocatalytic system by utilizing the defect-metal interaction in topological materials.

2 Experimental

2.1 Hydrothermal synthesis of Bi_2Se_3

0.1 mmol $C_{17}H_{33}COONa$, 0.01 mmol $InCl_3$, 0.02 mmol $BiCl_3$ and 0.045 mmol selenium were added into 30 mL of ethylene glycol with continuous stirring and sonication for 30 min. Then the mixture was transferred into a 50 mL Teflon-lined autoclave, sealed and heated at 160 °C for 6 h. Before the product was collected, it must be cooled down to room temperature naturally and washed with ethanol and water three times each. It was then dried in a vacuum for two days for further characterization.

2.2 Synthesis of Bi_2Se_3 with Se vacancies

The above Bi_2Se_3 was added into a porcelain boat and annealed under an Ar/H_2 atmosphere (0.8 kPa, 300 °C) for different hours to synthesize Bi_2Se_3 with Se vacancies, which were named V-Bi_2Se_3-1, V-Bi_2Se_3-3, and V-Bi_2Se_3-6 annealed at 1 h, 3 h, and 6 h, respectively.

3 Results and discussion

3.1 Structure and morphology

Fig. 1a presents the XRD patterns of Bi_2Se_3 and V-Bi_2Se_3-3, which exhibit nearly identical diffraction peaks consistent with the reference Bi_2Se_3 structure (PDF#33-0214). Distinct diffraction peaks at 18.56°, 25°, 29.36°, 40.26°, and 43.69° correspond to the (0 0 6), (1 0 1), (0 1 5), (1 0 10), and (1 1 0) crystallographic planes, respectively, confirming the characteristic hexagonal phase. Notably, thermal treatment at 300 °C under an Ar/H_2 atmosphere induces no detectable phase transformation, as evidenced by the preserved peak positions. The demonstrated thermal stability validates the material's applicability in elevated-temperature operational environments, with preservation of crystallographic integrity being essential for maintaining optimal catalytic activity and charge transport characteristics. The invariance of the diffraction patterns before and after heating further confirms the absence of lattice degradation or secondary phase formation. Scanning electron microscopy (SEM) characterization clearly reveals the ultrathin two-dimensional (2D) layered structure of Bi_2Se_3 (Fig. 1b). This unique morphology significantly increases the specific surface area, thereby effectively enhancing the number of active sites for catalytic reactions. Further studies demonstrate that the annealed V-Bi_2Se_3-3 sample exhibits slight surface curling (Fig. 1c), which can be attributed to the inherent structural relaxation effect of ultrathin 2D materials during high-temperature annealing.

To systematically investigate the structural evolution and interfacial characteristics of the catalysts, transmission electron microscopy (TEM) analysis was conducted. As evidenced by the high-resolution TEM (HRTEM) image in Fig. 1d, well-defined lattice fringes with spacings of 0.207 nm and 0.321 nm are observed on the nanosheets, corresponding to the (1 1 0) and (1 0 4) crystallographic planes of Bi_2Se_3 (PDF#17-0320), respectively. Significantly, a distinct set of lattice stripes with a spacing of 0.294 nm is identified, which aligns with the (1 1 1) plane of metallic bismuth (PDF#51-0765). This structural feature originates from the partial reduction of Bi^{3+} to Bi^0 during hydrogen-argon annealing at 300 °C, leading to the precipitation of metallic bismuth domains on the material surface. Such metallic phase segregation could substantially modulate electronic properties, including enhanced electrical conductivity and tailored catalytic selectivity. Definitive verification of elemental bismuth formation was achieved through energy-dispersive X-ray spectroscopy (EDS) mapping. Fig. 1e demonstrates a characteristic 100 nm particle within the yellow-circled region, exhibiting strong bismuth signals in both SEM-EDS elemental mapping and spectral analysis, confirming its identity as a metallic bismuth cluster. Furthermore, high-density nanoscale particulates distributed across the annealed surface (Fig. 1e inset) were unambiguously identified as metallic bismuth. These findings collectively demonstrate that thermal annealing induces surface reconstruction in bismuth selenide, generating bimetallic interfaces between Bi_2Se_3 and *in situ* formed Bi^0 clusters.

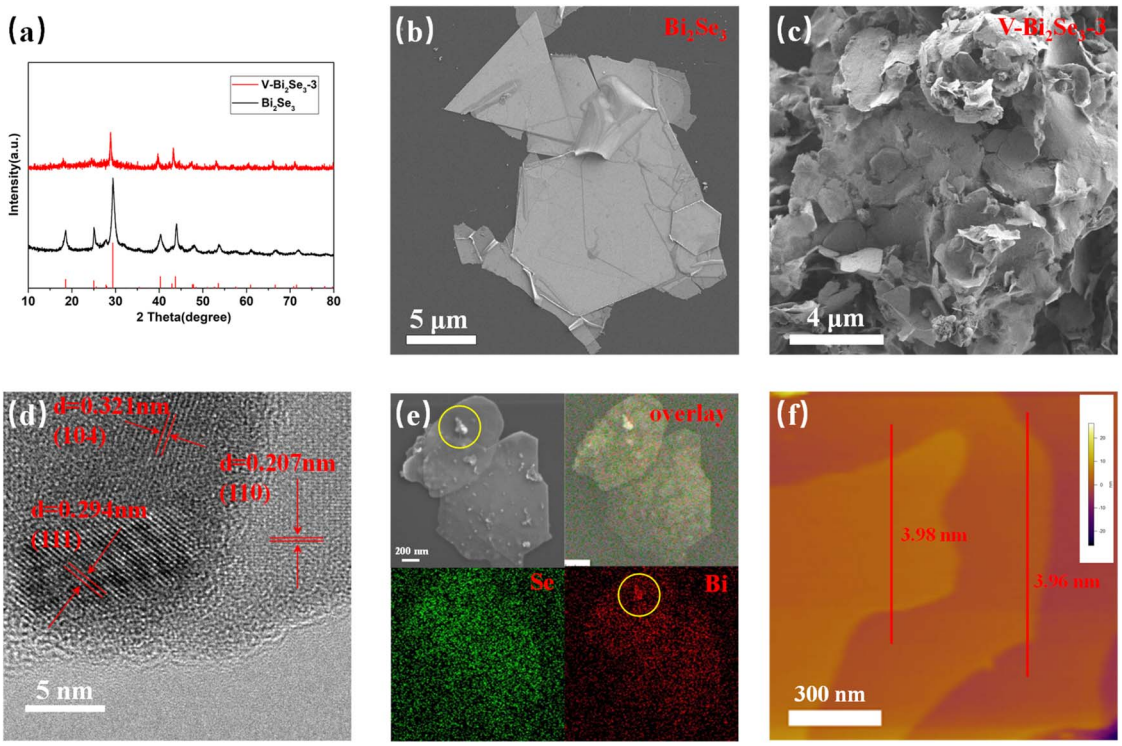

Fig. 1 (a) XRD spectra of Bi_2Se_3 and V-Bi_2Se_3-3; (b and c) SEM images of Bi_2Se_3 and V-Bi_2Se_3-3; (d) TEM images of V-Bi_2Se_3-3; (e) EDS mapping images of V-Bi_2Se_3-3; (f) AFM images of V-Bi_2Se_3-3.

To accurately characterize the geometric properties of the material, we employed atomic force microscopy (AFM) to evaluate the thickness distribution of the nanosheets. As shown in Fig. 1f, AFM topographic analysis reveals that the nanosheets exhibit an average thickness of 4.0 nm, consistent with the theoretical monolayer thickness of Bi_2Se_3 (~1.0 nm), indicating a four-atomic-layer stacking configuration. This sub-5-nm two-dimensional quantum confinement effect endows the material with three structural advantages: first, the ultrathin characteristic significantly reduces surface free energy, effectively maintaining structural integrity by suppressing atomic migration. Second, the confined interlayer distance (<1 nm) induces quantum confinement effects that not only protect surface active sites from oxidation/sintering-induced deactivation but also optimize catalytic cycle kinetics through enhanced interlayer electron transport. Furthermore, the unique layered structure effectively suppresses carbon deposition on the photocatalyst surface, attributed to its 2D confinement effect and ordered electron transport channels. These characteristics enable the catalyst to maintain high initial activity after prolonged continuous operation (Fig. S1), significantly improving the stability of the photocatalytic system.

The chemical structure and defect states of the samples were systematically analyzed using X-ray photoelectron spectroscopy (XPS) and electron paramagnetic resonance (EPR). As shown in Fig. 2a, the EPR spectrum of the V-Bi_2Se_3-3 sample exhibits a characteristic peak at a *g*-factor of 2.003, corresponding to Se vacancies, while no such signal is observed in the pre-annealed sample. This conclusively confirms the formation of thermally induced Se vacancies. These defect structures not only cause slight lattice distortions in the annealed sample but may also modulate its light-responsive capability by altering carrier concentrations. XPS analysis further reveals the evolution of the local chemical environment. The characteristic Bi^{3+} $4f_{7/2}$ and Bi^{3+} $4f_{5/2}$ peaks of pristine Bi_2Se_3 are located at 157.6 eV and 162.9 eV, respectively (Fig. 2b). In contrast, these peaks shift synchronously toward higher binding energies (158.1 eV and 163.4 eV) in the V-Bi_2Se_3-3 sample (Fig. 2c), indicating significant changes in the chemical coordination states of bismuth within the lattice. Combined with the metallic bismuth (Bi^0) peak observed at the *-marked position in Fig. 2c, these results confirm the partial reduction of Bi_2Se_3 to elemental Bi during annealing, leading to surface enrichment and interfacial interactions between metallic Bi and Bi_2Se_3. Simultaneously, the markedly reduced intensity of the Se 2p peaks corroborates the EPR findings, collectively supporting the conclusion that selenium vacancy formation causes depletion of Se atoms around Bi. The electronic structure reconfiguration driven by defect engineering, along with the emergence of surface metallic phases, may serve as a key mechanism for regulating the optoelectronic performance of the material.

In the high-frequency region of the Nyquist plot (in the small sub-figure of Fig. 2d, the region with relatively small coordinate values), the intersection point of the curve and the real axis approximately represents the solution resistance R_s. The equivalent circuit model for the Nyquist plot is provided in Fig. S2. The starting positions of the two materials in the high-frequency region are close, indicating that the solution

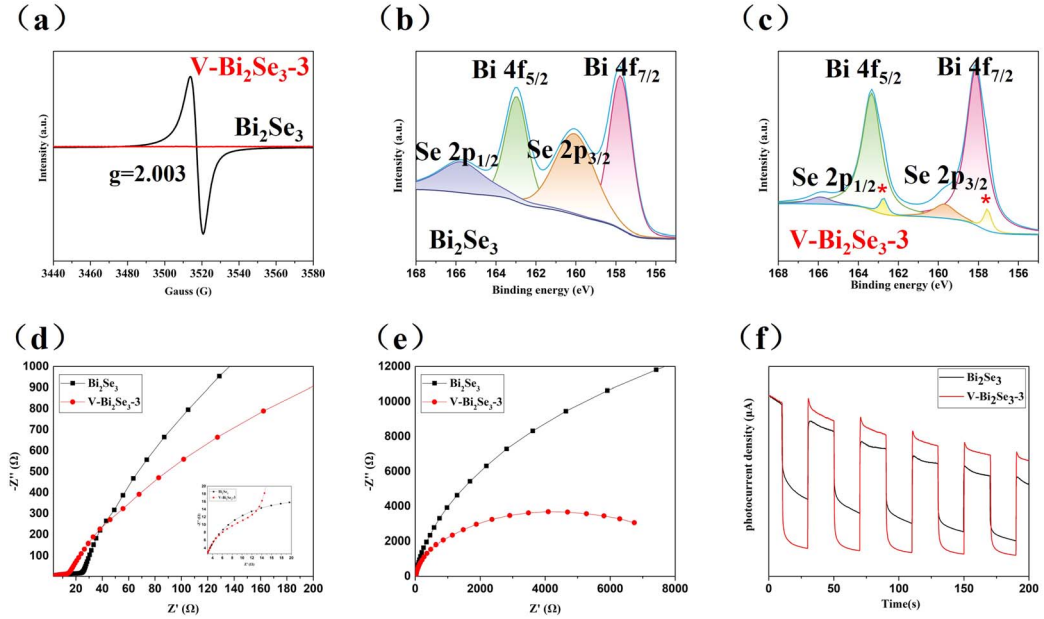

Fig. 2 (a) EPR spectra of Bi_2Se_3 and V-Bi_2Se_3-3; (b) XPS spectra of Bi_2Se_3 for Bi 4f and Se 2p; (c) XPS spectra of V-Bi_2Se_3-3 for Bi 4f and Se 2p; (d and e) impedance spectra of Bi_2Se_3 and V-Bi_2Se_3-3 in high, medium and low frequency regions; (f) photocurrent spectra of V-Bi_2Se_3-3.

resistances R_s of Bi_2Se_3 and V-Bi_2Se_3-3 have little difference. The solution resistance depends on the properties and concentration of the electrolyte, as well as the contact between the electrode and the electrolyte, suggesting that the electrolyte environments of the two materials have basically the same impact on the resistance. The intermediate-frequency region is usually related to the charge-transfer process, corresponding to the charge-transfer resistance R_{ct}. As can be observed from Fig. 2d, there are significant differences in the curves of Bi_2Se_3 and V-Bi_2Se_3-3 in the intermediate-frequency region. For the same Z′ value, the $-Z''$ value of Bi_2Se_3 is generally higher than that of V-Bi_2Se_3-3. The larger the charge – transfer resistance R_{ct}, the more difficult it is for charges to transfer at the electrode/electrolyte interface and the slower the electrode reaction kinetics. It is thus speculated that the charge-transfer resistance of Bi_2Se_3 is relatively large and the charge-transfer process is more difficult compared to V-Bi_2Se_3-3. This is because the Se vacancies in V-Bi_2Se_3-3 change the surface electronic structure of the material, promoting charge transfer. As can be seen from Fig. 2e, there are differences in the trends of the curves of the two materials in the low-frequency region. The curve of Bi_2Se_3 shows a more significant upward trend in the low-frequency region, while the curve of V-Bi_2Se_3-3 changes relatively gently. This implies that V-Bi_2Se_3-3 reduces the hindrance to charge diffusion and transfer in the system. All these findings prove that the formation of surface Se defects and the precipitation and attachment of surface elemental Bi are conducive to charge transfer.

As illustrated in Fig. 2f, the curves of photocurrent density as a function of time for Bi_2Se_3 (black curve) and V-Bi_2Se_3-3 (red curve) are presented. It is evident that, within each distinct time-cycle, the photocurrent density of V-Bi_2Se_3-3 consistently exhibits a higher value compared to that of Bi_2Se_3. This experimental outcome further serves as robust corroboration for the conclusion reached previously. That is, the charge-transfer process in V-Bi_2Se_3-3 is more favorable. In detail, in the case of V-Bi_2Se_3-3, the formation of surface Se defects disrupts the original electronic structure of the material, creating additional active sites. Meanwhile, the precipitation and attachment of surface elemental Bi modify the local electrical environment. These two factors act synergistically to significantly enhance charge transfer efficiency, thereby enabling photogenerated carriers to participate more effectively in photocatalytic reactions.

3.2 Photocatalytic activity

To evaluate the CO_2 reduction activity of the samples, we measured the CO yield rate in the atmosphere after light irradiation. Fig. 3a presents a line graph comparing the 6-hour photocatalytic CO_2 reduction performance of different samples, with the *x*-axis representing time (*h*) and the *y*-axis showing the CO yield rate (μmol g^{-1}). This graph demonstrates the significant influence of precursor annealing time on photocatalytic activity. While unannealed Bi_2Se_3 exhibits negligible activity, annealed samples with Se vacancies show markedly enhanced performance. Specifically, V-Bi_2Se_3-3 achieves a CO evolution yield of nearly 126.74 μmol g^{-1} in the first hour, significantly outperforming V-Bi_2Se_3-1 (50.2 μmol g^{-1}) and V-Bi_2Se_3-6 (40.10 μmol g^{-1}). However, excessive annealing (V-Bi_2Se_3-6) may introduce detrimental defects, adversely affecting light absorption and crystal morphology, thereby reducing activity. Fig. 3b displays the photocatalytic CO evolution rates under 300 W Xe lamp irradiation over 6 hours for the same samples. All samples exhibit increasing CO production with time, with V-Bi_2Se_3-3 showing the highest yield rate (29.34 μmol g^{-1} h^{-1}), followed by V-Bi_2Se_3-1 (17.84 μmol g^{-1} h^{-1}), V-Bi_2Se_3-6 (10.33 μmol g^{-1} h^{-1}) and pristine Bi_2Se_3 (1.07 μmol g^{-1} h^{-1}). This

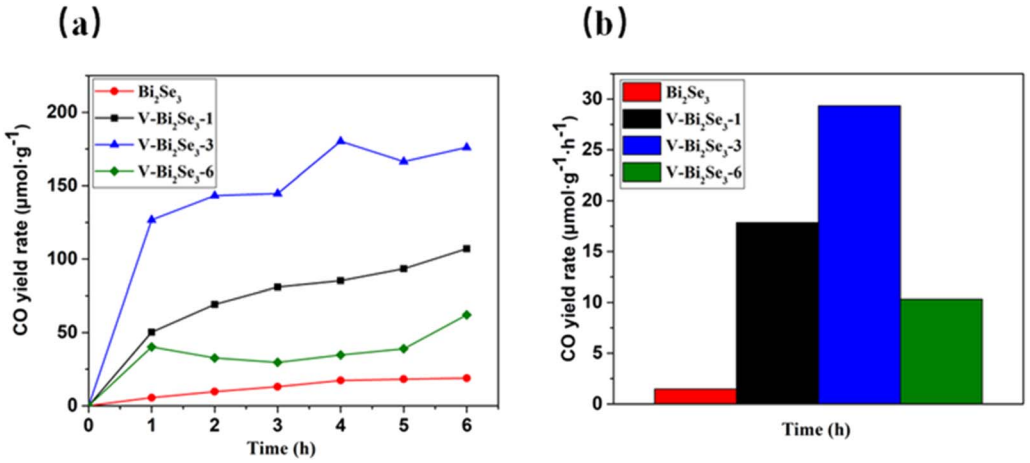

Fig. 3 (a) Photocatalytic CO evolution under 300 W Xe lamp irradiation for 6 h with different samples. (b) Comparison of the photocatalytic CO_2 reduction activity with different samples.

performance enhancement stems from the synergistic effects of Se vacancies and Bi clusters: (1) Se vacancies promote efficient electron-hole separation and strengthen CO_2 adsorption; (2) metallic Bi metal clusters serve as reactive sites to facilitate charge transfer, enhancing catalytic efficiency; and (3) the topological protection of Bi_2Se_3 nanosheets ensures structural stability while maintaining high conductivity, collectively optimizing charge dynamics. This dual-functional design-combining defect engineering with conductive bismuth clusters-not only maximizes catalytic activity but also ensures long-term durability. The steady increase in CO production confirms the photocatalysts' sustained activity, yet it also highlights the need for precise annealing optimization. Although Se vacancies initially enhance performance, excessive annealing (as in V-Bi_2Se_3-6) leads to activity degradation. These results emphasize the critical role of controlled synthesis conditions in maximizing the CO_2 reduction efficiency of Bi_2Se_3-based photocatalysts.

4 Conclusions

In summary, we synthesized selenium-vacancy-rich Bi_2Se_3 nanosheets with *in situ* formed bismuth metal clusters through a solvothermal method followed by hydrogen annealing. As an ultrathin topological insulator, Bi_2Se_3 maintains excellent electrical conductivity owing to its topological protection. The surface Se vacancies function as active centers for electron trapping and CO_2 molecule adsorption, while the Bi metal clusters serve as reactive sites to facilitate charge transfer and catalytic reactions. The optimized V-Bi_2Se_3-3 demonstrates outstanding photocatalytic CO_2 reduction performance, achieving a CO yield of nearly 130 μmol g^{-1}, significantly higher than that of unannealed samples. This work establishes that defect engineering coupled with *in situ* metal cluster formation constitutes an effective strategy to enhance the photocatalytic activity of topological insulators for CO_2 reduction, providing valuable insights for designing high-performance energy conversion materials.

Author contributions

The main contributions of the author of this paper are as follows: conceptualization: Yong Zhou put forward the idea of the subject. formal analysis: Yanjun Zhu and Qiutong Han analyzed the data and improved the experimental scheme; Yanjun Zhu analysed the SEM and TEM images. Investigation: Yanjun Zhu did the characterization test of the materials, then investigated and analyzed the literature. Resources: Yong Zhou provided the instruments used in the research. Writing – original draft: Yanjun Zhu wrote the initial draft. Writing – review & editing: Qiutong Han and Yong Zhou commented and revised the article.

Conflicts of interest

There are no conflicts to declare.

Data availability

The data included in this study are available from the corresponding author upon reasonable request.

Supplementary information is available. See DOI: **https://doi.org/10.1039/d5na00526d**.

Acknowledgements

The authors gratefully acknowledge the support from the National Key R&D Program of China (2024YFB4609400), the National Natural Science Foundation of China (Grant No. 224720022 and No. 22402079), the Natural Science Foundation of Jiangsu Province (BK20220006 and BK20230309), the Natural Science Foundation of the Jiangsu Higher Education Institutions of China (23KJB150015), the Provincial Talent Plan (Grant No. 2023TB0012), the Program from Guangdong Introducing Innovative and Entrepreneurial Teams (2019ZT08L101 and RCTDPT-2020-001), and the Shenzhen Key Laboratory of Eco-materials and Renewable Energy (ZDSYS20200922160400001).

Notes and references

1 X. Chang, T. Wang and J. Gong, *Energy Environ. Sci.*, 2016, **9**, 2177–2196.
2 A. Wagner, C. D. Sahm and E. Reisner, *Nat. Catal.*, 2020, **3**, 775–786.
3 D. Li, M. Kassymova, X. Cai, S.-Q. Zang and H.-L. Jiang, *Coord. Chem. Rev.*, 2020, **412**, 213262.
4 Q. Han, X. Bai, Z. Man, H. He, L. Li, J. Hu, A. Alsaedi, T. Hayat, Z. Yu, W. Zhang, J. Wang, Y. Zhou and Z. Zou, *J. Am. Chem. Soc.*, 2019, **141**, 4209–4213.
5 Q. Han, L. Li, W. Gao, Y. Shen, L. Wang, Y. Zhang, X. Wang, Q. Shen, Y. Xiong, Y. Zhou and Z. Zou, *ACS Appl. Mater. Interfaces*, 2021, **13**, 15092–15100.
6 M. Guan, C. Xiao, J. Zhang, S. Fan, R. An, Q. Cheng, J. Xie, M. Zhou, B. Ye and Y. Xie, *J. Am. Chem. Soc.*, 2013, **135**, 10411–10417.
7 W. Gao, S. Li, H. He, X. Li, Z. Cheng, Y. Yang, J. Wang, Q. Shen, X. Wang, Y. Xiong, Y. Zhou and Z. Zou, *Nat. Commun.*, 2021, **12**, 4747.
8 L. Wang, R. Wang, T. Qiu, L. Yang, Q. Han, Q. Shen, X. Zhou, Y. Zhou and Z. Zou, *Nano Lett.*, 2021, **21**, 10260–10266.
9 M. Liu, P. D. Spanos and S.-H. Yu, *Nano Energy*, 2019, **64**, 103877.
10 Y. Teng, L. L. Ning, C. W. Tan, J. Zhao, Y. W. Xiong, H. L. Zou, Z. M. Ye, X. M. Zhang, D. B. Kuang and Y. Li, *Adv. Funct. Mater.*, 2024, **35**, 2414892.
11 Y. Teng, Z. Zhou, J. Chen, S. Huang, H. Chen and D. Kuang, *Chin. Chem. Lett.*, 2025, **36**, 110430.
12 S. K. Das and P. Padhan, *Phys. Status Solidi B*, 2022, **259**, 2100516.
13 S. Noureen, S. U. Rehman, S. M. Batool, J. Ali, Q. Zhang, S. S. Batool, Y. Wang and C. Li, *ACS Appl. Mater. Interfaces*, 2024, **16**, 8158–8168.
14 R. Pan, J. Liu and J. Zhang, *ChemNanoMat*, 2021, **7**, 737–747.
15 A. T. Montoya and E. G. Gillan, *ACS Omega*, 2018, **3**, 2947–2955.
16 W. Ge, K. Liu, S. Deng, P. Yang and L. Shen, *Appl. Surf. Sci.*, 2023, **607**, 155036.
17 Y. Gao, J. Lin, Q. Zhang, H. Yu, F. Ding, B. Xu, Y. Sun and Z. Xu, *Appl. Catal., B*, 2018, **224**, 586–593.
18 L. Zhao, W. Fang, X. Meng, L. Wang, H. Bai and C. Li, *J. Alloys Compd.*, 2022, **910**, 164883.
19 K. Zhao, Z. Zhang, Y. Feng, S. Lin, H. Li and X. Gao, *Appl. Catal., B*, 2020, **268**, 118740.
20 H. Yu, J. Li, Y. Zhang, S. Yang, K. Han, F. Dong, T. Ma and H. Huang, *Angew. Chem., Int. Ed.*, 2019, **58**, 3880–3884.
21 L. Wang, D. Lv, F. Dong, X. Wu, N. Cheng, J. Scott, X. Xu, W. Hao and Y. Du, *ACS Sustainable Chem. Eng.*, 2019, **7**, 3010–3017.
22 Q. Chen, X. Cheng, H. Long and Y. Rao, *Chin. Chem. Lett.*, 2020, **31**, 2583–2590.
23 Y. Liu, B. Yang, H. He, S. Yang, X. Duan and S. Wang, *Sci. Total Environ.*, 2022, **804**, 150215.
24 M. Yang, X.-Q. Zhan, D.-L. Ou, L. Wang, L.-L. Zhao, H.-L. Yang, Z.-Y. Liao, W.-Y. Yang, G.-Z. Ma and H.-L. Hou, *Rare Met.*, 2024, **44**, 1024–1041.
25 L. Zhao, H. Hou, S. Wang, L. Wang, Y. Yang, C. R. Bowen, J. Wang, Z. Liao, D. Yang, R. Yan and W. Yang, *Adv. Funct. Mater.*, 2024, **35**, 2416346.
26 H. Hou, C. R. Bowen, D. Yang and W. Yang, *Chem*, 2024, **10**, 800–831.
27 Y. Zong, H. Chen, J. Wang, M. Wu, Y. Chen, L. Wang, X. Huang, H. He, X. Ning, Z. Bai, W. Wen, D. Zhu, X. Ren, N. Wang and S. Dou, *Adv. Mater.*, 2023, **35**, 2306269.
28 C. Fan, K. Sakamoto and P. Krüger, *Appl. Surf. Sci.*, 2024, **643**, 158699.
29 Z. Sun, T. Liu, Q. Shen, H. Li, X. Liu, H. Jia and J. Xue, *Appl. Surf. Sci.*, 2023, **616**, 156530.